Nano Energy (2015) 18, 187–195

Available online at www.sciencedirect.com

ScienceDirect

journal homepage: www.elsevier.com/locate/nanoenergy

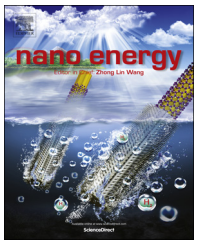

RAPID COMMUNICATION

Formation of mono/bi-layer iron phosphate and nucleation of $LiFePO_4$ nano-crystals from amorphous 2D sheets in charge/discharge process for cathode in high-performance Li-ion batteries

Tongchao Liu[a,1], Yancong Feng[a,1], Yandong Duan[a], Suihan Cui[a], Lingpiao Lin[a], Jiangtao Hu[a], Hua Guo[a], Zengqing Zhuo[a], Jiaxin Zheng[a], Yuan Lin[a], Wanli Yang[a,c], Khalil Amine[a,b], Feng Pan[a,*]

[a]*School of Advanced Materials, Peking University Shenzhen Graduate School, Shenzhen 518055, China*
[b]*Electrochemical Technology Program, Chemical Sciences and Engineering Division, Argonne National Laboratory, Argonne, IL 60439, United States*
[c]*Advanced Light Source, Lawrence Berkeley National Laboratory, Berkeley, CA 94720, United States*

Received 5 September 2015; received in revised form 14 October 2015; accepted 17 October 2015
Available online 31 October 2015

KEYWORDS
2D-sheets;
H-bond network;
Nano-crystals;
Transmission line model

Abstract
We prepared mono/bi-layer iron phosphate two-dimensional (2D) materials with 0.74 nm/1.52 nm thickness by means of a simple chemically induced precipitation method and post-processing. The mechanism of growth of the atomically thin 2D-sheet crystals was investigated by experimental measurements and theoretical calculations. The crystalline 2D sheets were easily oxidized to the amorphous phase in air, and $LiFePO_4$ nano-crystals self-nucleated from amorphous 2D sheets in the charge/discharge process. The 2D sheets show excellent performance properties as cathode materials: high initial discharge capacity of 185 mAh g^{-1} at 0.1 C, stable cycling (98% capacity retention over 400 cycles), and high rate capability (107 mAh g^{-1} at 20 C) for Li-ion storage. A model for self-nucleation of the $LiFePO_4$ nano-crystals involving double-center diffusion is discussed.

*Corresponding author.
E-mail address: panfeng@pkusz.edu.cn (F. Pan).
[1]These authors contributed equally to this work.

http://dx.doi.org/10.1016/j.nanoen.2015.10.016
2211-2855/

Introduction

Since first reported by Goodenough in 1997 [1], $LiFePO_4$, has been commercially used as the cathode material of Li-ion batteries (LIB) because of its high theoretical capacity with high voltage, capacity retention under long charge/discharge cycling, safety, low toxicity, and low cost. Many methods, such as metal doping [2-5], carbon coating on particle surfaces [6-10], and particle scaling to nano-size [11-17] have been developed to improve the electrochemical properties of $LiFePO_4$ to overcome its low electronic conductivity and low Li-ion transportability. The approach of forming nano-sized $LiFePO_4$ particles has been intensively investigated to create shorter paths and larger implantation surface areas for fast Li-ion diffusion to enhance the charge/discharge rate for high-power density applications, such as electric vehicles [18].

Since graphene was reported by Geim and Novoselov et al. [19] in 2004, two-dimensional (2D) layered materials (sheets) that are a few layers thick, such as metal chalcogenides [20-21], transition metal oxides [22], and other two-dimensional compounds [23], have rapidly risen to be one of the hottest topics in material science due to their attractive properties for various applications [24-27]. These 2D sheets can be combined with weak interactions between adjacent layers (e.g., van der Waals interactions and hydrogen bonds) and with strong interactions (e.g., covalent bonding within a layer) [28]. These 2D sheets with one to a few atomically thin layers display interesting properties due to their strong anisotropic features with high specific surface areas and are being explored for various applications such as optoelectronics [29], catalysts [30,31], supercapacitors [32], solar cells [33,34], and lithium-ion batteries [35-37].

Results and discussion

For this paper, we synthesized mono/bi-layer iron phosphate in 2D sheets with 0.74–1.52 nm thickness, and investigated the mechanism of growth of the atomically thin 2D-sheet crystals by experimental measurements and theoretical calculations. Self-nucleation of $LiFePO_4$ nano-crystals from the oxidation amorphous 2D-sheets in the air during charge/discharge process is found with ex-situ by transmission electron microscopic (TEM) and in-situ by electrochemical impedance spectroscopy (EIS). These 2D-sheets also show high performances as cathode materials for LIBs.

These atomically thin amorphous 2D sheets are controllably prepared through a simple chemically induced precipitation method and post-processing (see Experimental section for details). The formation mechanism was determined by experimental measurements and theoretical calculations. The three main fabrication steps are represented in Figure 1 and discussed below.

In step 1, the iron phosphate precursor is formed with ethylene glycol (EG) coated around the surfaces. To begin, $FeSO_4 \cdot 7H_2O$, H_3PO_4, and $LiOH \cdot H_2O$ are mixed by stirring for about 6 h at room temperature, resulting in an amorphous cotton-like material ("precursor" shown in Figures 1 and S1). The X-ray diffraction (XRD) pattern shows that the precursor is amorphous and exhibits no crystalline diffraction peak (Figure 2a). Inductively coupled plasma-atomic emission spectrometry (ICP-AES) shows that the elements of the amorphous cotton-like precursor has a Li/Fe/P atomic ratio of ca. 0.2:1.4:1, while gas chromatography-mass spectrometry (GC–MS) indicates the precursor has a large amount of EG molecules. This was confirmed by fourier transform infrared (FTIR) spectra, in which the peak around

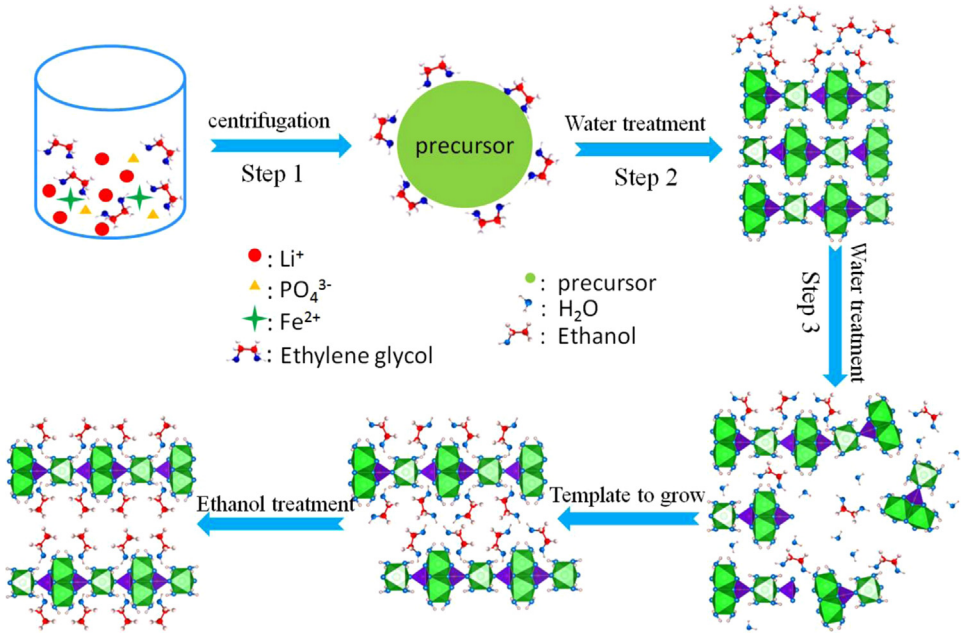

Figure 1 Schematic for formation of atomically thin 2D sheets of amorphous iron phosphate. The process involves conversion of precursor to $Fe_3(PO_4)_2 \cdot 8H_2O$ crystal by water treatment, exfoliation of $Fe_3(PO_4)_2 \cdot 8H_2O$ molecules by the mixture of water and ethylene glycol (EG), formation of new hydrogen bonds with the EG molecules, and formation of the 2D sheets. The 2D sheets are further washed by ethanol to generate $Fe_3(PO_4)_2 \cdot 8H_2O$ thin films without agglomeration.

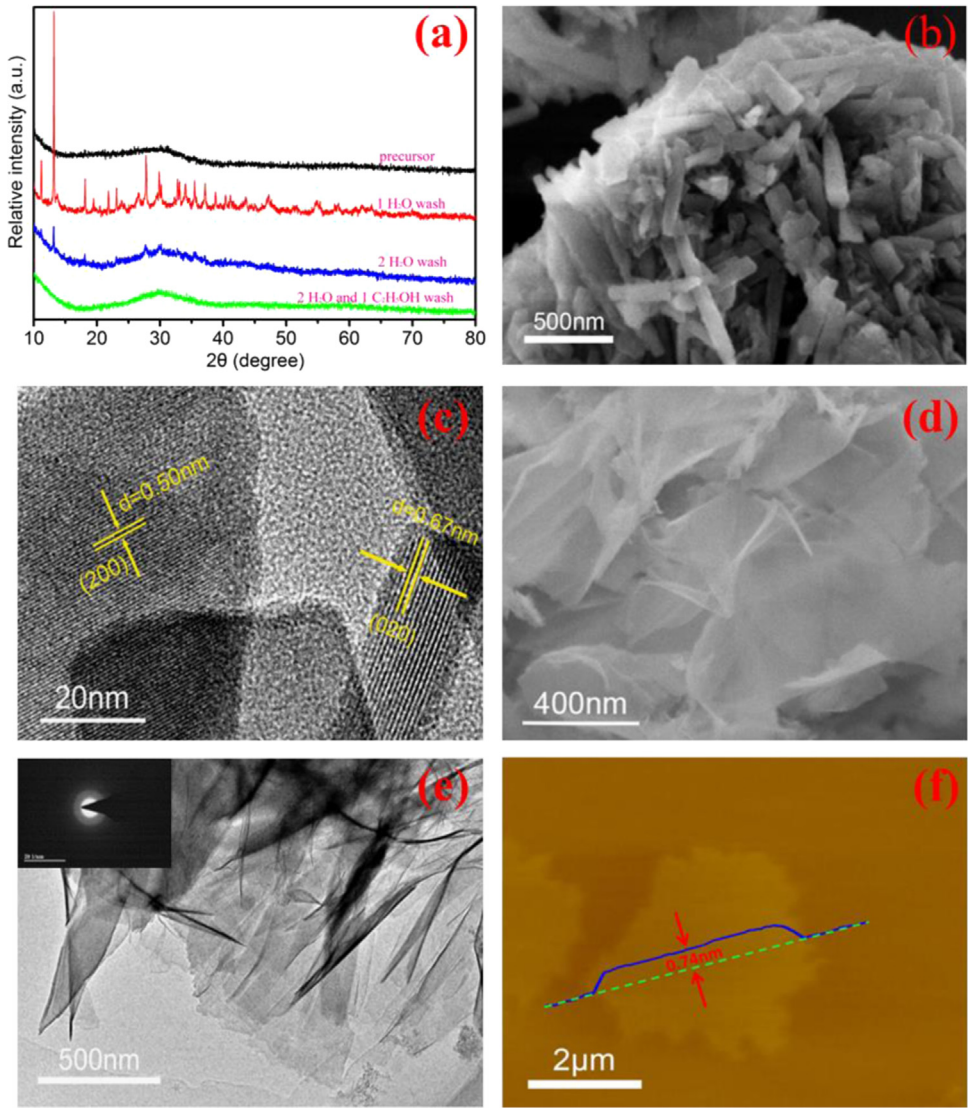

Figure 2 (a) XRD of samples for different treatments of the original precursor: water wash one time, water wash two times, and water wash two times plus ethanol wash one time. (b) SEM images of the product after washing with deionized water one time, $Fe_3(PO_4)_2 \cdot 8H_2O$ nano-crystalline particles. (c) High-resolution TEM (HR-TEM) image of $Fe_3(PO_4)_2 \cdot 8H_2O$ particles showing the lattice fringes of (020) and (200) planes. (d) SEM images of the product after deionized water wash two times and ethanol washing one time. (e) TEM image of the atomically thin 2D-sheets. The inset is selected area electron diffraction image of the 2D sheets. (f) AFM image of a typical nanosheet with a thickness of 0.74 nm, corresponding to one atomic layer.

2860–2960 cm^{-1} is related to the C–H stretching vibration and that at 3200–3400 cm^{-1} is related to the O–H stretching vibration (Figure S2). Meanwhile, thermogravimetric (TG) analysis (Figure S3) shows that the total weight loss of about 34.7% takes place mainly around 30–400 °C, which can be attributed to the evaporation of EG around the surfaces of the precursor. Note that the evaporation point of EG is only about 190 °C, but the temperature of the weight loss for the EG-coated precursor occurs near 400 °C. This difference may be due to the stronger interactions at the precursor-EG interface with chemical coordination bonding occurring between OH groups of EG and Fe(II) cations of the precursor.

In Step 2, $Fe_3(PO_4)_2 \cdot 8H_2O$ nano-crystalline particles are generated when the precursor is washed with deionized water for the first time (Figures 1 and 2a and b). The XRD measurement confirms that the nano-crystal is tetragonal $Fe_3(PO_4)_2 \cdot 8H_2O$, matched with the standard JCPDS card no. 30-0662 (space group I2/m (12), a = 10.034 Å, b=13.449 Å, c=4.707 Å). The $Fe_3(PO_4)_2 \cdot 8H_2O$ crystal has a layer structure, in which the layers of $Fe_3(PO_4)_2$ are constructed by Fe-O octahedra linking to phosphate P-O tetrahedra. The interlayers of $Fe_3(PO_4)_2$ are linked with hydrogen bonds through eight water molecules, which are coordinated with an iron atom through an oxygen atom as shown in Figures 1 and S4. The high-magnification transmission electron microscopy (TEM) images (Figure 2c) reveal two kinds of obvious lattices in the $Fe_3(PO_4)_2 \cdot 8H_2O$ nano-crystals. The interplanar distances of 0.67 nm and 0.50 nm fit well with the plane distance of d_{020} and d_{200}, respectively. We also observed that the surfaces of the $Fe_3(PO_4)_2 \cdot 8H_2O$ nano-crystals are

coated with EG molecules to form $Fe_3(PO_4)_2 \cdot 8H_2O@EG_x$ (subscript x is the molar ratio of EG to $Fe_3(PO_4)_2 \cdot 8H_2O$, equaling 2.7). That observation is confirmed by the GC–MS and FTIR spectra, as well as the TG data (Figures S5 and S6). Note that the value of x is directly proportional to the surface area of the nano-crystals.

In Step 3, atomically thin iron phosphate 2D-sheet crystals and amorphous material are formed (Figures 1 and 2a). For this step, the $Fe_3(PO_4)_2 \cdot 8H_2O@EG_x$ nano-crystals are washed by deionized water to become $Fe_3(PO_4)_2 \cdot 8H_2O@EG_y$ thin films (y should be less than x due to the water washing), followed by washing with ethanol to generate $Fe_3(PO_4)_2 \cdot 8H_2O@EtOH_z$ thin films without agglomeration, as shown in Figure 2d (see discussion below). By measurements with an elemental analyzer, as well as TG and energy dispersive X-ray spectroscopy (EDS) mapping, the values of y and z in $Fe_3(PO_4)_2 \cdot 8H_2O@EG_y$ and $Fe_3(PO_4)_2 \cdot 8H_2O@EtOH_z$ were estimated to be 0.606 and 0.767, respectively (see Table S1 and Figures S7 and S8). The TEM images in Figure 2e indicate that the as-prepared thin films with ethanol washing are amorphous sub-nanometer sheets without electron diffraction spots in the selected area. High-resolution TEM images clearly illustrate no crystal lattice (Figure S9) to further prove the amorphous structure of the as-prepared thin films. The thicknesses of the thin films measured by atomic force microscopy (AFM) are ~0.74 nm and ~1.52 nm, as shown in Figures 2f and S10. These films are thus 2D sheets with mono/bi-layer thickness of the $Fe_3(PO_4)_2 \cdot 8H_2O$ along (020). To determine the 2D-sheet material composition, we employed XRD, soft X-ray absorption spectroscopy (XAS), and X-ray photoelectron spectroscopy (XPS). The XRD pattern shows no crystalline diffraction peak, indicating an amorphous material. The soft XAS shows that the 2D-sheet materials contain Fe(II) and Fe(III) peaks (Figure S11). The XPS (Figure S12) is in agreement with the soft XAS. The proposed mechanism is that the Fe(III) signal results from the oxidation of Fe(II) in $Fe_3(PO_4)_2 \cdot 8H_2O$ to produce $Fe(III)_3(PO_4)_2(OH)_3$, in which for the conservation of charge, Fe(III) must alter to coordinate with the OH^- to replace H_2O. According to the ICP-AES result of Fe/P atomic ratio of ca. 3.05:2.07, the composition of the amorphous 2D sheets is $Fe(II)_3(PO_4)_2 \cdot Fe(III)_3(PO_4)_2(OH)_3 \cdot nH_2O@EtOH_z$. Because of the oxidation, the original crystal structure of the $Fe_3(PO_4)_2 \cdot 8H_2O$ thin films is broken up to become amorphous 2D sheets.

We now turn to the mechanism that accounts for the growth of the mono/bi-layer 2D-sheet crystal of $Fe_3(PO_4)_2 \cdot 8H_2O$ during the water washing process. Experimental results show that the EG on the 2D-sheet surfaces is stable and not washed away by water, indicating the strong interactions between EG and the 2D sheet. First-principle theoretical calculations show two possible models for one EG molecule with two H_2O molecules on the crystal interface, as shown in Figure S13. For model I in Figure S13a, one hydroxy of the EG molecule in the interface region connects with two H_2O molecules bonded with different Fe(II) atoms on the (020) surface of $Fe_3(PO_4)_2 \cdot 8H_2O$ crystal. This forms two kinds of H-bonds, with H-bond length d_{O-H} 1.734 Å and 1.780 Å, respectively. For model II in Figure S13b, both hydroxyls of one EG are adsorbed to form three types of hydrogen bonds with the two H_2O molecules, and the related d_{O-H} lengths are 1.792 Å, 1.700 Å, and 1.714 Å, respectively. The binding energies of the two adsorption models are −1.13 eV and −1.20 eV, respectively. The binding energy of absorption with one H_2O on the (020) surface of $Fe_3(PO_4)_2 \cdot 8H_2O$ is −0.77 eV, which is much less than that of the former two models with EG. Therefore, EG can be strongly bonded on the crystal surface to replace H_2O.

As shown Figure 3, the $Fe_3(PO_4)_2 \cdot 8H_2O$ molecule at the edge of the crystal/EG interface is named “Cluster A”, while that in the solution is called “Cluster B”. One EG molecule would become the “co-center” for many H-bonds to link “Cluster A” and “Cluster B” for the thin film crystal growth along the “crystal/EG/solution interface template”. Note that the $Fe_3(PO_4)_2 \cdot 8H_2O$ molecules without EG covering the edges of the nano-crystals could be corroded during the water washing, and then diffuse nearby to the crystal/EG/solution interface to grow along the surface layer directions

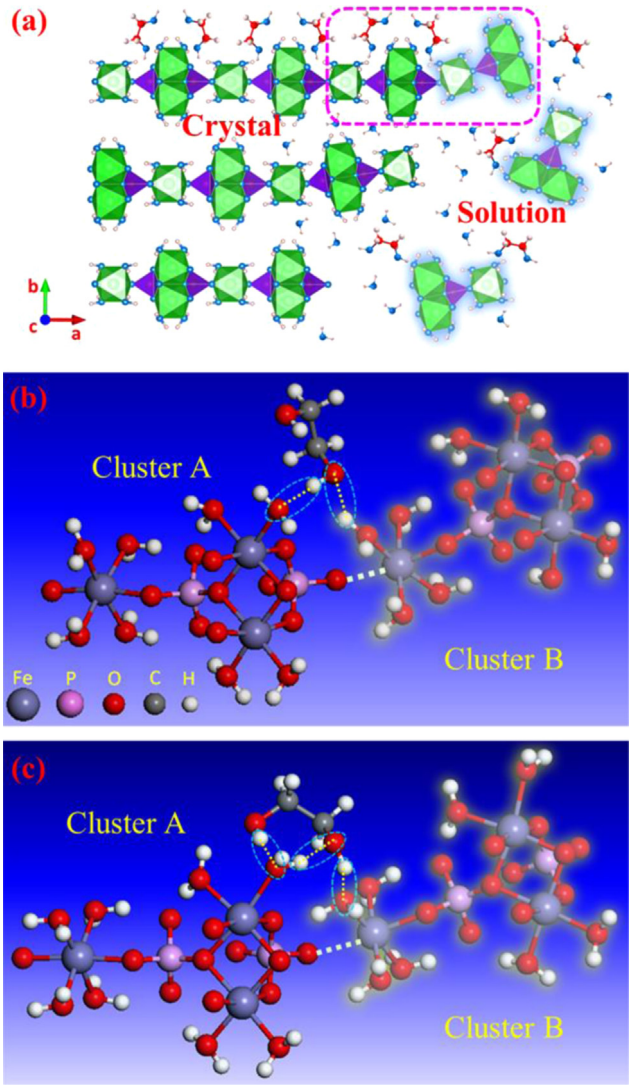

Figure 3 (a) Model of the growth of $Fe_3(PO_4)_2 \cdot 8H_2O$ nanosheets. The green units represent Fe–O octahedra, and the purple units represent P–O tetrahedra. The section bounded by dashed lines is amplifed in images below: (b) Model I of H-bond network and (c) Model II of H-bond network.

of the nano-crystals, generating 2D-sheet crystals as shown in Figure 3. We hypothesized that the growth of atomically thin crystals is the result of three key factors. The first concerns the $Fe_3(PO_4)_2 \cdot 8H_2O$/EG interface with the H-bond network: the OH groups of EG molecules strongly H-bond with H_2O molecules in $Fe_3(PO_4)_2 \cdot 8H_2O$ (see Figure 3a). Second, the strong H-bond network of EG and H_2O in solution is also built around the crystal/EG interfaces. The third concerns the "template" for the 2D-sheet crystal growth: according to factors (1) and (2), the hydrated $Fe_3(PO_4)_2$ in the solution, as a growing unit, diffuses to the "template", while the "template" also supplies the seed surface for crystal growth continuously along the (200) and (002) direction. By theoretical calculations and experimental measurements, we determined that the crystal/EG/solution interface template controls the 2D-sheet crystal growth along the interface of the crystal and EG, in which one EG as the co-center bridges one H_2O molecule from Cluster A at the crystal surface and another H_2O molecule from Cluster B in solution with multiple H-bonds.

The 2D-sheet crystals are agglomerated in EG, which can be attributed to the H-bond network of EG to link the sheets. The 2D sheets can be de-agglomerated by washing with ethanol. The mechanism was investigated by expertiments and theortical calculations as below. After being washed with ethanol, these 2D sheets are coated with ethanol in a proportion of about 6.56% ($Fe_3(PO_4)_2 \cdot 8H_2O@EtOH_z$, $z=0.767$) of the total weight, as confirmed by the elemental analyzer and TG (Table S1 and Figure S14). Forthermore, the high-resolution C1s X-ray photoelectron spectroscopy (XPS) spectrum of the composite (Figure S15) was used to measure different chemical environments of carbon atoms, such as C-C (284.6 eV) and C-O (286.2 eV), indicating that the percentage of carbon with C-C and C-O of the 2D sheets is 47.5% and 44.4%, respectively. Thus, the surface material coated on the 2D sheets is ethanol, which can replace EG during the washing. By first principles calculation, the binding energy of the ethanol molecule on the (020) surface of $Fe_3(PO_4)_2 \cdot 8H_2O$ is strong, -1.19 eV, which is greater than -1.13 eV (model I) and close to -1.20 eV (model II) for EG molecules. Thus, ethanol can replace EG to become the coating molecules to generate the $Fe_3(PO_4)_2 \cdot 8H_2O@EtOH_z$ for 2D sheets.

The surface of the nano-crystals of $Fe_3(PO_4)_2 \cdot 8H_2O$ and 2D sheets of $Fe_3(PO_4)_2 \cdot 8H_2O@EtOH_z$ is oxidized in air from Fe(II) in $Fe_3(PO_4)_2 \cdot 8H_2O$ to Fe(III) in the new composition, as confirmed by the measurements of soft XAS and XPS (Figures S11 and S12), respectively. As a result, the original 2D-sheet crystals are easily changed into amorphous 2D sheets, which we used for investigation of the electrochemistry and performance of cathode materials in Li-ion coin cells.

To fully explore the electrochemical performance, we mixed the atomically thin 2D sheets with carbon black by ball milling for about 4 h with the mass ratio of 5:3. The SEM images and EDS mapping show that the 2D sheets and carbon black had been fully mixed together as Fe$(II)_3(PO_4)_2 \cdot Fe(III)_3(PO_4)_2(OH)_3 \cdot nH_2O$/C ("FP@C") (Figures S16 and S17). The electrochemical performance of the FP@C composite was tested as a cathode in a coin cell, in which lithium metal was used as the counter electrode.

Figure 4a shows that the first discharge capacity was high, about 185 mAh g^{-1} at the 0.1 C. Note that because of the absence of lithium ion, Fe(II) in FP@C is oxidized to Fe(III) in the first charge with a capacity of about 49 mAh g^{-1}. However, after the second charge/discharge cycle, the electrode delivers a stable reversible capacity of 184, 182, 174, 142, 127, and 109 mAh g^{-1} at 0.1 C, 0.5 C, 1 C, 5 C, 10 C, and 20 C, respectively. The cell also shows good cycling stability: the capacity rises to 175 mAh g^{-1} at 1 C after cycling from 0.1 C to 20 C (Figure 4c). The long-term cycling stability at a 10 C rate is also excellent; as shown in Figure S18, the capacity retention is about 97%, declining only slightly from 122 mAh g^{-1} at the 1st cycle to 118 mAh g^{-1} at the 400th cycle. The excellent rate capability and electrochemical reversibility can mainly be attributed to the cathode material having atomically thin 2D-sheet features, in which the blockage of Li-ion diffusion in the bulk electrode material is broken through during the fast charge/discharge. The mechanism of how and where to store Li-ions during charge/discharge cycles for atomically thin amorphous FP@C 2D-sheets is further investigated as below. The cyclic voltammogram (CV) curves show significant differences between the first and the second charge/discharge cycle (Figure 4b). The first cycle is an active process for the electrode, in which the oxidation from Fe(II) to Fe(III) occurs during the charging, and reduction from Fe(III) to Fe(II) occurs with intercalating Li ions to the 2D sheets, resulting in high polarization redox potential. After the second cycle, the CV curves are stable with a pair of current peaks positioned at 3.25 V and 2.87 V, respectively, corresponding to the redox of Fe(III)/Fe(II).

The Li-ion diffusion kinetic features were investigated by further CV testing with different scan rates from 0.1 mV s^{-1} to 5 mV s^{-1}. The shapes of these CV curves (Figure 4d) are similar without distortion whatever the scan rate, meaning that the 2D sheets provide excellent rate capability. We assume that the current obeys a power-law relationship with the scan rate [38], $I_p = av^b$, where a and b are adjustable values. A b value of 0.5 indicates that the current is controlled by semi-infinite linear diffusion, while a b value of 1 indicates that the current is surface controlled like capacitance. We derived a b value of 0.819-0.912 through fitting the logarithmic relationship between sweep rate and current at different voltages (Figure 4d). Therefore, the 2D sheets as the Li-ion cathode behave more like capacitance with surface-controlled current during the charge/discharge process, which can be attributed to the ultra-high interface areas and atomically thin path of the 2D sheets for Li-ion diffusion (Figure S19). Note that the reversible capacity at 0.1 C is about 185 mAh g^{-1} as shown in Figure 4a, which is higher than the theoretical capacity of $LiFePO_4$ (170 mAh g^{-1}). Actually, the reversible capacity of 2D-sheet cathodes consists of three parts: lithium storage in amorphous 2D sheets, lithium storage in $LiFePO_4$ nano-crystals, and capacitance, so that the extra-capacity could result from the part of contribution of capacitance due to the large surfaces of the 2D sheets. Also note that the charge/discharge curve is the slope, instead of the typical plateau of the olivine phosphate, which could result from the most part of the reversible capacity contributed from "capacitance-like" contribution of the amorphous 2D sheets.

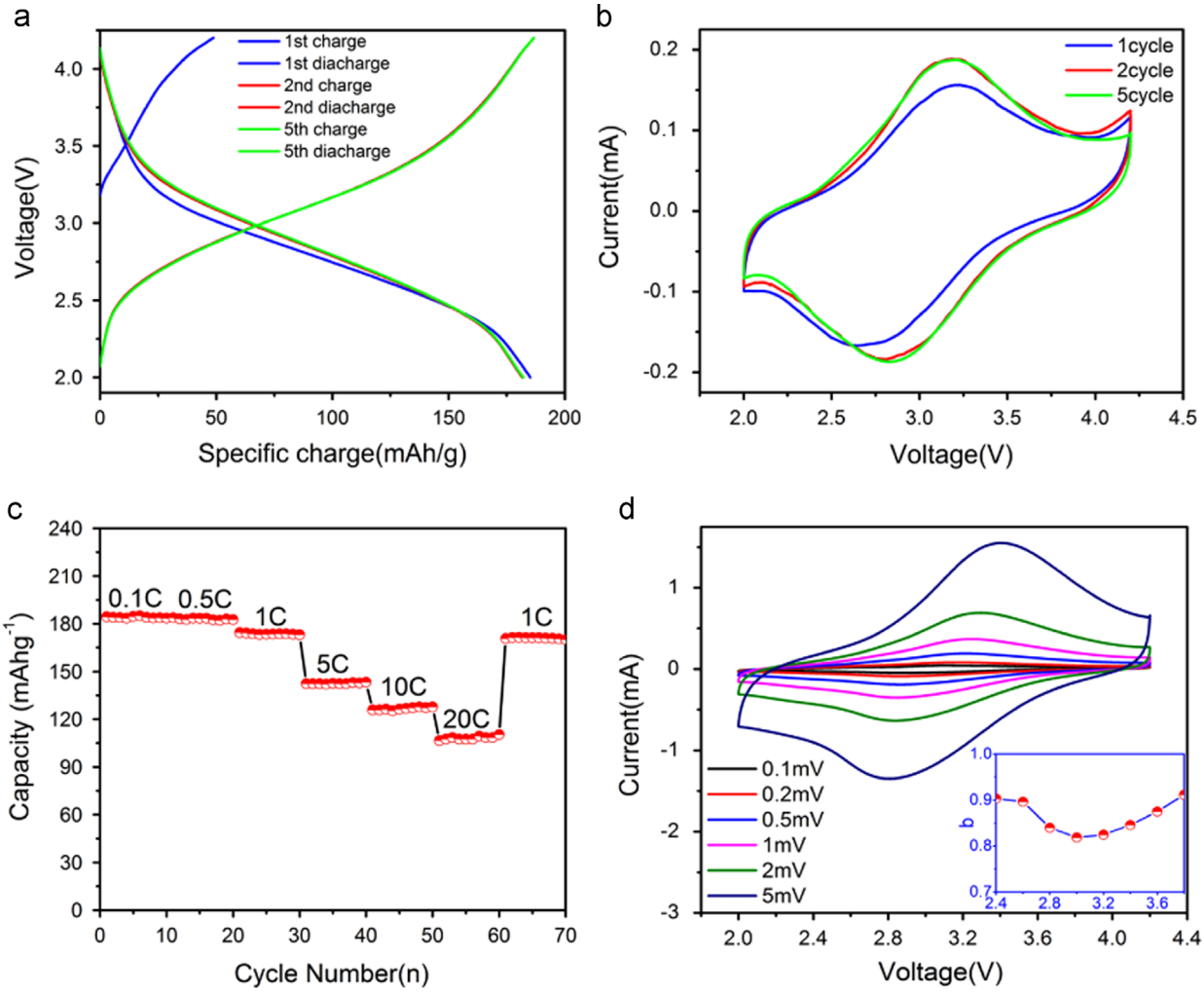

Figure 4 (a) Galvanostatic discharging/charging profiles obtained at 0.1 C. (b) CV curves obtained at a scan rate of 0.1 mV s^{-1} (voltage window 2.0–4.2 V). (c) Capacity versus cycle number at different discharge rates. (d) CV curves conducted at scan rates of 0.1 mV s^{-1} to 5 mV s^{-1}.

Electrochemical impedance spectroscopy (EIS) was performed after 1, 20, and 100 cycles at 1 C, as shown in Figure 5a. The visible semicircles in the high and middle frequency ranges reflect the solid-electrolyte interface (SEI) resistance (R_{sei}) and charge transfer resistance (R_{ct}), respectively. The EIS plots for these 2D-sheet cathodes have two features. The first is that the second semicircle appears with charge/discharge cycles, indicating that a new "second-phase" is generated. The second is the decrease of resistance with cycling, which is different than the increase of resistance during cycling typical of crystalline materials.

To investigate the second phase generated after cycling, we dismantled the coin cell after 1000 cycles at 10 C and cleaned the electrode materials for TEM and XRD analyses. Figure 5b shows the XRD patterns of the electrode materials with strong reflection peak at 44.8°, which corresponds to the phase structure of (122) planes of crystalline $LiFePO_4$. The electrode materials were further characterized by TEM (Figure 5c), in which many nano-crystal particles with 5–8 nm sizes are found inside of the 2D sheets. The high-magnification TEM images revealed the obvious lattice channels in the nano-particles with an interplanar distance of about 0.21 nm. This finding is consistent with the d_{122} value (0.21 nm) calculated from the XRD pattern of $LiFePO_4$ crystals. Thus, both TEM and XRD results strongly support the contention that $LiFePO_4$ nano-crystals can be self-generated as new Li-ion storage centers from atomically thin iron phosphate amorphous 2D sheets in the charge/discharge process. The $LiFePO_4$ nano-crystals are self-nucleated only from domains with $LiFePO_4$-like short-ordering structures in the amorphous 2D sheets. However, it is difficult to grow the nano-crystals larger due to the higher mobility resistance of the iron phosphate group in the solid amorphous region. Note that the ratio of $LiFePO_4$ nano-crystals self-nucleated and amorphous part left without nucleation cannot be defined. Although the ratio between Fe and P in $LiFePO_4$ is 1:1, the balance of Fe:P in the amorphous part is difficult to clarify.

Hence, in the EIS curves, both the appearance of the second semicircle and decrease of resistance during cycling can be attributed to the generation of $LiFePO_4$ nano-crystals from the amorphous 2D sheets to make electrode materials

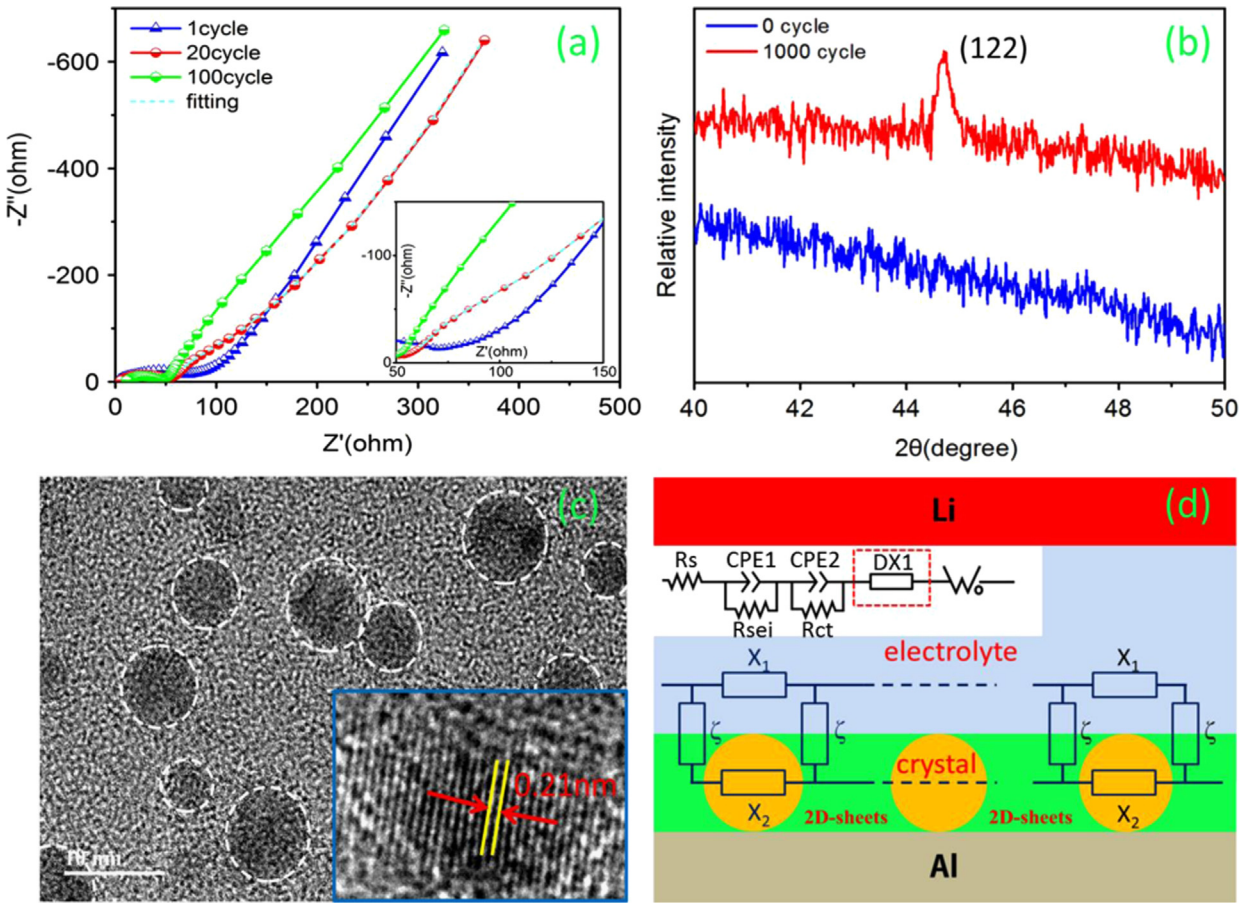

Figure 5 (a) Electrochemical impedance spectroscopy (EIS) for 1, 20, and 100 charge/discharge cycles. The inset is the enlarged figure of EIS. (b) XRD pattern for crystallization of nanosheets after 1000 cycles. (c) HR-TEM image for crystallization of 2D sheets. The inset is the enlarged figure of nano-crystals. (d) Schematic illustration for the transmission line model. The equivalent circuit is characterized by the elements X_1, X_2, and ζ. The impedance X_1 is that of the liquid paths, X_2 is that of the solid network, and ζ is the impedance of the solid/liquid interface.

having amorphous and crystal phases, respectively. The "transmission line model" (Figure 5d) is proposed to simulate EIS features, in which Li ions in the amorphous 2D sheets can diffuse into the amorphous phase, electrolyte, and $LiFePO_4$ nano-crystalline particles during charge/discharge. The EIS data in Figure 5a fit well with the transmission line model, in which Li-ion diffusion inside of the amorphous phase is different from that in the $LiFePO_4$ nanoparticles. Therefore, the second semicircle of the EIS curves occurs when $LiFePO_4$ nano-crystals are nucleated as second phases. Furthermore, Li-ion diffusion in the new phase of $LiFePO_4$ nanoparticles is faster than that in the amorphous region, leading to the decrease of resistance during cycling.

Conclusions

In summary, mono- and bi-layer $Fe_3(PO_4)_2 \cdot 8H_2O$ 2D-sheet crystals have been formed by the mechanism of growth of a "crystal/EG/solution interface template". The $Fe_3(PO_4)_2 \cdot 8H_2O$ nano-crystals are etched while the 2D-sheet crystals grow along the crystal/EG/solution interface. The $Fe_3(PO_4)_2 \cdot 8H_2O$ 2D-sheet crystals coated with ethanol are oxidized into the amorphous iron phosphate 2D sheets in air. The thickness of the 2D sheet is about 0.74 nm and 1.52 nm with one and two atomic layers, respectively. The formation of only a monolayer or bilayer of 2D sheets can be attributed to the stronger binding energy between crystal and EG than that between crystal and water. In coin cell tests, the 2D-sheet cathodes attained a high reversible capacity of 185 mAh g^{-1} and 109 mAh g^{-1} at 0.1 C and 20 C, respectively. They also showed excellent rate capability. Interestingly, the new phases, $LiFePO_4$ nano-crystals, are self-nucleated with about 5 nm sizes during the charge/discharge cycles, which become new Li-ion storage sites. Hence, this work indicates that the atomically thin 2D-sheets can be used as novel electrode materials with hybrid behavior of battery and supercapacitor for a super performance Li-ion battery.

Materials and methods

Material preparation

All the reagents were purchased from Sinopharm Chemical Reagent Co., Ltd., and used without further purifying. Atomically thin two-dimensional nanosheet precursors of amorphous iron phosphate were prepared by a chemically

induced precipitation method. Firstly, 0.85 g of $LiOH \cdot H_2O$ and 1.10 g of H_3PO_4 were dissolved in 83.25 g and 16.67 g of ethylene glycol, respectively. Next, 2.09 g of $FeSO_4 \cdot 7H_2O$ and 0.11 g of ascorbic acid were dissolved in 66.67 g of ethylene glycol. The solution of a $FeSO_4 \cdot 7H_2O$ and ascorbic acid was added to a 250 ml three-necked flask under stirring and aerated in a nitrogen atmosphere for 0.5 h to remove the oxygen in the solution. Then, the H_3PO_4 solution was added slowly to a $FeSO_4 \cdot 7H_2O$/ascorbic acid solution under vigorous stirring. After reaction for about 15 min, $LiOH \cdot H_2O$ solution was added slowly to the prior mixed solution. After reaction for about 6 h, we obtained the precursor by precipitation with a centrifuge.

Characterization

X-ray powder diffraction patterns were obtained by using a Bruker D8 Advance diffractometer with Cu Kα (λ=0.15418 nm). The diffraction data were recorded in the 2θ range of 10–80° with a step of 0.02° and a count time of 1 s. The morphologies of the materials were observed by SEM (ZEISS Supra 55) and TEM (FEI Tecnai G2 F20 S-Twin). Also, EDS maps were recorded by using an Oxford-Max20 detector attached to the SEM. Thermogravimetry analysis data were collected on a TGA/DSC1 system at a heating rate of 10 °C/min under oxygen flow. The thickness of the nanosheet was determined by AFM (Bruker MultiMode 8). Infrared spectroscopy to verify the presence of water and ethylene glycol was conducted on a SHIMADZU IR Prestige-21. The presence of ethylene glycol was verified by GC/MS, and the elemental components of the material were analyzed by ICP-AES (Horiba Jobinyvon JY2000-2). The surface area was determined by nitrogen adsorption/desorption using the Brunauer–Emmett–Teller method (BET, Micromeritics ASAP 2020 HD88).

Electrochemical measurements

Electrochemical characterization was carried out with 2032 coin cells. The working electrode was prepared by coating aluminum foil with a slurry of active material (50 wt%), carbon black (30 wt%), and poly(vinylidene fluoride) binder (20 wt%) dissolved in N-methylpyrrolidine. The slurry was dried in vacuum at 110 °C for 12 h. The electrolyte consisted of 1 M $LiPF_6$ in a mixture of ethylene chloride, diethyl chloride, and dimethyl chloride with a volume ratio of 1:1:1. All the cells were assembled in a glove box with water/oxygen content lower than 1 ppm and tested at room temperature. The galvanostatic discharging–charging tests were conducted on a NEWARE battery cycler in the voltage range of 2.0–4.2 V (vs. Li^+/Li) at room temperature. The CV results were recorded by a CHI 604E (ChenHua Instruments Co., China). The electrochemical impedance spectra were recorded from 10^4 to 0.1 Hz, and the amplitude of the used perturbation was 10 mV.

Modeling

Density functional theory (DFT) calculations were performed using the projector-augmented wave methods implemented in the Vienna ab initio simulation package (VASP). The Perdew-Burke-Ernzerhof (PBE) form of the generalized gradient approximation (GGA) was selected as the exchange-correlation potential. The PBE+U approach was employed to consider the strong on-site Coulomb interaction (U) presented in the localized 3d electrons of Fe, with the U value equal to 5.3, according to the website (https://www.materialsproject.org). The plane wave energy cutoff was set to 520 eV. The maximum residual force was less than 0.02 eV/Å. A primitive cell of bulk vivianite $Fe_3(PO_4)_2 \cdot 8H_2O$ was fully relaxed with a k-point mesh of $3 \times 3 \times 3$. For the calculation of adsorption energy, the (020) surface was modeled by a slab with a vacuum region greater than 20 Å. The k-point mesh was set to be $3 \times 1 \times 5$. The adsorption energy is expressed by $E_a = E_{c/m} - E_c - E_m$, where $E_{c/m}$, E_c and E_m are the energy of the adsorbed system, $Fe_3(PO_4)_2 \cdot 8H_2O$ crystal, and mole cule (such as water, EG, and EtOH), respectively.

Acknowledgments

The work was financially supported by Guangdong Innovation Team Project (No. 2013N080), Shenzhen Science and Technology Research Grant (ZDSY20130331145131323, KYPT20141016105435850).

Appendix A. Supplementary material

Supplementary data associated with this article can be found in the online version at http://dx.doi.org/10.1016/j.nanoen.2015.10.016.

References

[1] A.K. Padhi, K.S. Nanjundaswamy, J.B. Goodenough, J. Electrochem. Soc. 144 (1997) 1188–1194.
[2] S.Y. Chung, J.T. Bloking, Y.M. Chiang, Nat. Mater. 1 (2002) 123–128.
[3] N.N. Bramnik, K.G. Bramnik, K. Nikolowski, M. Hinterstein, C. Baehtz, H. Ehrenberg, Electrochem. Solid State 8 (2005) 379–381.
[4] K.L. Harrison, C.A. Bridges, M.P. Paranthaman, C.U. Segre, J. Katsoudas, V.A. Maroni, J.C. Idrobo, J.B. Goodenough, A. Manthiram, Chem. Mater. 25 (2013) 768–781.
[5] B. Rong, Y. Lu, X. Liu, Q. Chen, K. Tang, H. Yang, X. Wu, F. Shen, Y. Chen, Y. Tang, Y. Chen, Nano Energy 6 (2014) 173–179.
[6] C.-Z. Lu, G.T.-K. Fey, H.-M. Kao, J. Power Sources 189 (2009) 155–162.
[7] L. Wang, G.C. Liang, X.Q. Ou, X.K. Zhi, J.P. Zhang, J.Y. Cui, J. Power Sources 189 (2009) 423–428.
[8] X.-L. Wu, L.-Y. Jiang, F.-F. Cao, Y.-G. Guo, L.-J. Wan, Adv. Mater. 21 (2009) 2710–2714.
[9] J. Wang, X. Sun, Energy Environ. Sci. 5 (2012) 5163–5185.
[10] J. Zheng, Y. Hou, Y. Duan, X. Song, Y. Wei, T. Liu, J. Hu, H. Guo, Z. Zhuo, L. Liu, Z. Chang, X. Wang, D. Zherebetskyy, Y. Fang, Y. Lin, K. Xu, L. Wang, Y. Wu, F. Pan, Nano Lett. (2015) (published online).
[11] K. Saravanan, P. Balaya, M.V. Reddy, B.V.R. Chowdari, J.J. Vittal, Energy Environ. Sci. 3 (2010) 457–464.
[12] K. Saravanan, M.V. Reddy, P. Balaya, H. Gong, B.V.R. Chowdari, J.J. Vittal, J. Mater. Chem. 19 (2009) 605–610.

[13] Y. Zhao, L. Peng, B. Liu, G. Yu, Nano Lett. 14 (2014) 2849–2853.
[14] G. Kobayashi, S.-i Nishimura, M.-S. Park, R. Kanno, M. Yashima, T. Ida, A. Yamada, Adv. Funct. Mater. 19 (2009) 395–403.
[15] J. Wang, J. Yang, Y. Tang, J. Liu, Y. Zhang, G. Liang, M. Gauthier, Y.C. Chen-Wiegart, M. Norouzi Banis, X. Li, R. Li, J. Wang, T.K. Sham, X. Sun, Nat. Commun. 5 (2014) 3415.
[16] J. Jiang, W. Liu, J. Chen, Y. Hou, A.C.S. Appl., Mater. Inter 4 (2012) 3062–3068.
[17] N. Meethong, H.-Y.S. Huang, W.C. Carter, Y.-M. Chiang, Electrochem. Solid State 10 (2007) 134–138.
[18] P. Xiong, L. Peng, D. Chen, Y. Zhao, X. Wang, G. Yu, Nano Energy 12 (2015) 816–823.
[19] K.S. Novoselov, A.K. Geim, S.V. Morozov, D. Jiang, Y. Zhang, S.V. Dubonos, I.V. Grigorieva, A.A. Firsov, Science 306 (2004) 666–669.
[20] Y. Wang, J. Ou, S. Balendhran, A.F. Chrimes, M. Mortazavi, D.D. Yao, M.R. Field, K. Latham, V. Bansal, J.R. Friend, S. Zhuiykov, N.V. Medhekar, M.S. Strano, K. Kalantar-zadeh, ACS Nano 7 (2013) 10083–10093.
[21] J.A. Miwa, M. Dendzik, S.S. Grønborg, M. Bianchi, J.V. Lauritsen, P. Hofmann, S. Ulstrup, ACS Nano 9 (2015) 6502–6510.
[22] W.J. Ong, L.L. Tan, S.P. Chai, S.T. Yong, A.R. Mohamed, Nanoscale 6 (2014) 1946–2008.
[23] Y. Liu, X. Zou, B.I. Yakobson, ACS Nano 6 (2012) 7053–7058.
[24] D. Teweldebrhan, V. Goyal, A.A. Balandin, Nano Lett. 10 (2010) 1209–1218.
[25] T. Yao, L. Liu, C. Xiao, X. Zhang, Q. Liu, S. Wei, Y. Xie, Angew. Chem. 52 (2013) 7554–7558.
[26] C. Wu, X. Lu, L. Peng, K. Xu, X. Peng, J. Huang, G. Yu, Y. Xie, Nat. Commun. 4 (2013) 2431.
[27] C. Schliehe, B.H. Juarez, M. Pelletier, S. Jander, D. Greshnykh, M. Nagel, A. Meyer, S. Foerster, A. Kornowski, C. Klinke, H. Weller, Science 329 (2010) 550-3.
[28] G. Eda, H. Yamaguchi, D. Voiry, T. Fujita, M. Chen, M. Chhowalla, Nano Lett. 11 (2011) 5111–5116.
[29] W. Choi, M.Y. Cho, A. Konar, J.H. Lee, G.B. Cha, S.C. Hong, S. Kim, J. Kim, D. Jena, J. Joo, S. Kim, Adv. Mater. 24 (2012) 5832–5836.
[30] K. Jin, J. Park, J. Lee, K.D. Yang, G.K. Pradhan, U. Sim, D. Jeong, H.L. Jang, S. Park, D. Kim, N.E. Sung, S.H. Kim, S. Han, K.T. Nam, J. Am. Chem. Soc. 136 (2014) 7435–7443.
[31] Y. Sun, S. Gao, F. Lei, J. Liu, L. Liang, Y. Xie, Chem. Sci. 5 (2014) 3976–3982.
[32] L. Peng, X. Peng, B. Liu, C. Wu, Y. Xie, G. Yu, Nano Lett. 13 (2013) 2151–2157.
[33] M. Tsai, S. Su, J. Chang, D. Tsai, C. Chen, C. Wu, L. Li, L. Chen, J. He, ACS Nano 8 (2014) 8317–8322.
[34] P. Qin, G. Fang, W. Ke, F. Cheng, Q. Zheng, J. Wan, H. Lei, X. Zhao, J. Mater. Chem. A 2 (2014) 2742–2756.
[35] J. Wan, W. Bao, Y. Liu, J. Dai, F. Shen, L. Zhou, X. Cai, D. Urban, Y. Li, K. Jungjohann, M.S. Fuhrer, L. Hu, Adv. Energy Mater. 5 (2015) 1401742.
[36] Y. Li, H. Zhu, F. Shen, J. Wan, S. Lacey, Z. Fang, H. Dai, L. Hu, Nano Energy 13 (2015) 346–354.
[37] Y. Hou, J. Li, Z. Wen, S. Cui, C. Yuan, J. Chen, Nano Energy 8 (2014) 157–164.
[38] J. Come, P.L. Taberna, S. Hamelet, C. Masquelier, P. Simon, J. Electrochem. Soc. 158 (2011) 1090–1093.